

# Enhanced annealing stability of ferrimagnetic Tb/FeCo multilayers

Cite as: AIP Advances **11**, 085112 (2021); <https://doi.org/10.1063/5.0055817>

Submitted: 05 May 2021 . Accepted: 12 July 2021 . Published Online: 06 August 2021

 Michael Heigl, Chayangkoon Mangkornkarn,  Aladin Ullrich, et al.

## COLLECTIONS

 This paper was selected as an Editor's Pick



View Online



Export Citation



CrossMark

## ARTICLES YOU MAY BE INTERESTED IN

[Determination of anisotropy constants via fitting of magnetic hysteresis to numerical calculation of Stoner–Wohlfarth model](#)

AIP Advances **11**, 085111 (2021); <https://doi.org/10.1063/5.0051454>

[The design and verification of MuMax3](#)

AIP Advances **4**, 107133 (2014); <https://doi.org/10.1063/1.4899186>

[Utilizing spin currents from the dual surfaces of a heavy metal Pt layer for simultaneous spin-torque switching in FeTb/Pt/FeTb trilayers](#)

Applied Physics Letters **118**, 212406 (2021); <https://doi.org/10.1063/5.0042252>

Call For Papers!

AIP Advances

**SPECIAL TOPIC:** Advances in  
Low Dimensional and 2D Materials

# Enhanced annealing stability of ferrimagnetic Tb/FeCo multilayers

Cite as: AIP Advances 11, 085112 (2021); doi: 10.1063/5.0055817

Submitted: 5 May 2021 • Accepted: 12 July 2021 •

Published Online: 6 August 2021



View Online



Export Citation



CrossMark

Michael Heigl,<sup>1,a)</sup>  Chayangkoon Mangkornkarn,<sup>1</sup> Aladin Ullrich,<sup>1</sup>  Michal Krupinski,<sup>1,2</sup>   
and Manfred Albrecht<sup>1</sup> 

## AFFILIATIONS

<sup>1</sup>Institute of Physics, University of Augsburg, 86159 Augsburg, Germany

<sup>2</sup>Institute of Nuclear Physics, Polish Academy of Sciences, 31342 Krakow, Poland

<sup>a)</sup>Author to whom correspondence should be addressed: [michael.heigl@uni-a.de](mailto:michael.heigl@uni-a.de)

## ABSTRACT

In this study, we have investigated amorphous 20-nm-thick Tb/Fe<sub>80</sub>Co<sub>20</sub> multilayer samples with different individual layer thicknesses and their corresponding alloy counterpart. In particular, the structural and magnetic properties were analyzed upon post-annealing. Up to a certain critical thickness of the individual layers in the multilayer, no significant difference between the multilayers and the alloy is observed in their as-deposited states, which indicates the importance of interfacial intermixing. With a further increase in thicknesses of the individual layers, regions with significant larger Tb content emerge, resulting in a reduced effective Tb moment. The loss in perpendicular magnetic anisotropy upon annealing seems to be delayed for multilayers with thin individual layers compared to the alloy sample. We contribute this behavior to the underlying anisotropic short-range order enforced by the multilayer structure, which hinders the structural relaxation process. At higher temperatures, the multilayers strongly intermix and Fe and Co diffuse through the capping layer. This process leads to a strong enhancement of the saturation magnetization at a certain annealing temperature, due to the formation of separated FeCo and Tb-rich TbFeCo alloy layers, until the sample gets oxidized.

© 2021 Author(s). All article content, except where otherwise noted, is licensed under a Creative Commons Attribution (CC BY) license (<http://creativecommons.org/licenses/by/4.0/>). <https://doi.org/10.1063/5.0055817>

## I. INTRODUCTION

Ferrimagnetic (FI) heavy rare earth (RE)-3d transition metal (TM) alloys provide high tunability of magnetic properties, such as saturation magnetization and perpendicular magnetic anisotropy (PMA),<sup>1–7</sup> and can exhibit zero magnetic moment at the compensation temperature  $T_{\text{comp}}$  depending on the alloy composition. PMA is mainly associated with a chemical short-range order,<sup>8,9</sup> where RE-TM atom pairs prefer an out-of-plane direction. These properties make them a compelling material candidate for a variety of applications. For instance, the use of ferrimagnetic RE-TM systems as pinning layers for soft ferromagnetic (FM) films is of high interest.<sup>10–18</sup> In this regard, the switching behavior of the soft layer has been intensely studied and led to the term *exchange-spring magnets*,<sup>10</sup> which has further implications for spintronic devices, such as spin valves<sup>19–24</sup> and magnetic tunnel junctions.<sup>25</sup> Furthermore, all-optical switching of magnetic domains in GdFeCo thin films<sup>26</sup> induced by fs-laser pulses was discovered, and many intriguing works

on the ultrafast magnetization reversal in TbFe(Co) followed.<sup>27–30</sup> In addition, ferrimagnetic RE-TM materials have been utilized in THz technologies,<sup>31–35</sup> allowing thermomagnetic control of spintronic THz emitters.<sup>36</sup>

Moreover, many studies have also been devoted to ferrimagnetic multilayers (MLs) because of their additional tunability of magnetic anisotropy depending on their individual layer thicknesses.<sup>9,37–43</sup> Recently, also optical switching of magnetization in a ferrimagnetic Tb/Co multilayer was investigated with an explicit focus on the annealing stability.<sup>44,45</sup> In addition, by tailoring the magnetic properties of Fe/Gd multilayers, it was demonstrated that it is possible to stabilize various topologically protected spin objects, such as skyrmions<sup>46</sup> and antiskyrmions,<sup>47</sup> solely by dipolar interactions, which might be highly beneficial for skyrmionic memory devices.<sup>48,49</sup> However, the presented multitude of possible applications benefits or even requires thermal stability. Despite the fact that RE-TM systems provide intriguing tunable magnetic properties, they also exhibit irreversible changes upon annealing already

occurring at temperatures as low as 450 K in TbFeCo,<sup>50,51</sup> which is much lower than their crystallization temperature.<sup>1,52,53</sup> On the other hand, it was also reported that annealing procedures at temperatures up to 500 K can be used to increase PMA in TbFeCo films.<sup>54,55</sup>

In this study, we have investigated the influence of the multi-layer structure of Tb/FeCo on the structural and magnetic properties depending on the annealing temperature and compare the results to their alloy counterparts. Having a detailed understanding of the underlying processes upon annealing is crucial for future spintronic devices operating at elevated temperatures.

## II. EXPERIMENTAL DETAILS

Three different  $[\text{Tb}(t_{\text{Tb}})/\text{Fe}_{80}\text{Co}_{20}(t_{\text{FeCo}})]_N$  MLs were investigated with  $t_{\text{Tb}} = 0.40, 0.79, 1.27$  nm;  $t_{\text{FeCo}} = 0.37, 0.74, 1.23$  nm; and  $N = 26, 13, 8$ , respectively. The thicknesses and repetition numbers were chosen to replicate the corresponding composition and thickness of a 20-nm-thick  $\text{Tb}_{28}(\text{Fe}_{80}\text{Co}_{20})_{72}$  alloy thin film. Note that the provided thicknesses are nominal thicknesses. A schematic of the ML stack and the corresponding alloy is depicted in Fig. 1. The films were deposited at room temperature (RT) by dc magnetron (co-)sputtering (chamber base pressure  $<10^{-8}$  mbar) from elemental targets. The sample holder rotates during the deposition to achieve a uniform film composition. The Ar sputter pressure was kept constant at  $5 \times 10^{-3}$  mbar during the deposition process. The Tb, Fe, and Co deposition rates were 0.079, 0.060, and 0.014 nm/s, respectively. The films were prepared on Si(100) substrates with a 100-nm-thick thermally oxidized  $\text{SiO}_x$  layer. 5 nm Pt were used as the seed layer to enhance the PMA of the ferrimagnetic films.<sup>56,57</sup> The system was capped by 5 nm Ta or Pt to prevent oxidation. The individual layer thicknesses were adjusted by the deposition rate, which was controlled by a calibrated quartz balance. The composition and thickness of the alloy were confirmed by Rutherford backscattering spectrometry using 2 MeV  $\text{He}^+$  ions at a scatter angle of  $170^\circ$ . It is important to note that the physical properties of TbFeCo alloys are very sensitive to small variations in composition and deposition conditions.<sup>1,8,58</sup> Thus, all presented samples were prepared under the same conditions and magnetron configuration.

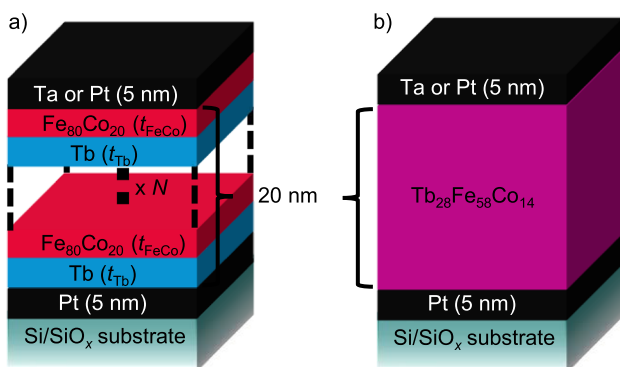


**FIG. 1.** Schematic image illustrating the layer stacking of Tb/FeCo MLs (a) and the corresponding  $\text{Tb}_{28}(\text{Fe}_{80}\text{Co}_{80})_{72}$  (20 nm) alloy (b). The used individual layer thicknesses and repetitions are  $t_{\text{Tb}} = 0.40, 0.79, 1.27$  nm;  $t_{\text{FeCo}} = 0.37, 0.74, 1.23$  nm; and  $N = 26, 13, 8$ , respectively.

To investigate the thermal stability of the samples, they were annealed in the nitrogen atmosphere at 430, 570, 640, and 720 K using a constant heating rate of 2 K/min. After reaching the final temperature, the heater was immediately switched off and the sample cooled down.

The integral magnetic properties of the samples were investigated by superconducting quantum interference device-vibrating sample magnetometry (SQUID-VSM). Magnetization vs external magnetic field ( $M-H$ ) hysteresis loops were captured in out-of-plane (oop) and in-plane (ip) geometry at RT. All samples were measured before and after annealing. It has been shown that edge effects can lead to artifacts in the measured  $M-H$  hysteresis loops.<sup>59</sup> Thus, their occurrence was prevented by cutting off all edges of the measured samples. The effective magnetic anisotropy  $K_{\text{eff}}$  was determined from the integrated area difference between the oop and ip  $M-H$  hysteresis loops. In order to confirm the Tb dominant nature of the investigated film samples, their remanent magnetization vs temperature ( $M_{\text{R}}-T$ ) curves were measured. The samples were saturated at RT in an oop field of +7 T, cooled down while the field was still applied, and measured with a guiding field of +10 mT with increasing temperatures from 40 to 340 K. Magnetic force microscopy (MFM) was used to receive information about the magnetic domain morphology at RT. To access the equilibrium domain size, the samples were first demagnetized by decaying alternating magnetic fields.

In addition to the magnetic measurements, we have investigated the structural changes using four-point resistivity measurements. During these measurements, the samples were annealed in the nitrogen atmosphere at a rate of 2 K/min up to 720 K. Cross-sectional transmission electron microscopy (TEM) samples were prepared by mechanical dimpling followed by ion polishing. High-angle annular dark-field scanning transmission electron microscopy (HAADF-STEM) imaging and spectrum imaging analysis based on energy-dispersive x-ray spectroscopy (EDS) were performed at an accelerating voltage of 200 kV on a JEOL NeoArm F200 system to obtain the element composition and to analyze interface intermixing upon annealing. Additional high-resolution TEM images were taken to judge the crystallinity of the individual layers. The overall crystal structure of the films was characterized by x-ray diffraction (XRD) using  $\text{Cu-K}\alpha$  radiation. The XRD patterns were measured in the  $\Theta - 2\Theta$  geometry with a  $2^\circ$  tilt angle to reduce the Bragg reflection intensity of the mono-crystalline Si(100) substrate.

## III. RESULTS AND DISCUSSION

### A. Magnetic properties

First, we compared the magnetic properties of the prepared MLs and the alloy thin film. All  $M-H$  hysteresis loops showed strong PMA with an easy axis of magnetization pointing in the oop direction as will be discussed later. The obtained  $M_{\text{R}}-T$  curves are plotted in Fig. 2. The TbFeCo alloy exhibits a declining absolute value of remanent magnetization (saturation magnetization) with temperature, which indicates a Tb dominant system. There is no  $T_{\text{comp}}$  in the measured temperature range, but it is expected at around 450 K by extrapolation. The curves of the two MLs with thinner individual layers ( $N = 26, 13$ ) match the curve of the alloy very well. The results of the alloy and the two thinner MLs are consistent with studies reported in the literature for similar systems.<sup>1</sup>

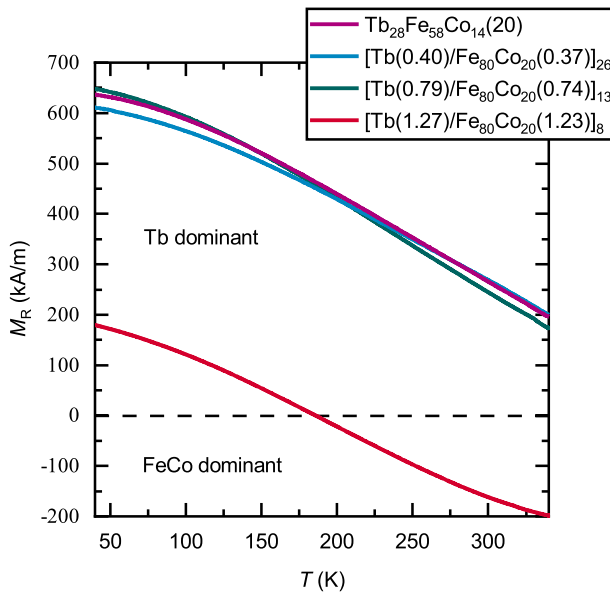


**FIG. 2.** Remanent magnetization  $M_R$  vs temperature  $T$  curves recorded with a guiding field of +10 mT. The curves of the two MLs with thinner individual layers ( $N = 26, 13$ ) match the curve of the alloy very well and are Tb dominant over the whole measured  $T$  range. The ML with the thickest individual layers ( $>1$  nm) reveals a magnetic compensation point  $T_{\text{comp}}$  at 190 K. All thicknesses are given in nm.

The ML with the thickest individual layers shows a curve similar in shape but with a negative offset of roughly 400 kA/m. Due to the smaller effective Tb moment, this sample is only Tb dominant up to 190 K at which the two sub-lattices compensate each other ( $T_{\text{comp}}$ ). At  $T > 190$  K, the sample's FeCo sub-lattice is magnetically dominant. It has been shown that interlayer intermixing plays an important role in Tb/Fe multilayers.<sup>60,61</sup> If the individual layer thicknesses surpass the intermixing thicknesses, the RE-TM ratio is significantly modulated along the film normal. The threshold has been reported to be around 1 nm.<sup>38,60</sup> This explains the discrepancy between  $[\text{Tb}(1.27)/\text{Fe}_{80}\text{Co}_{20}(1.23)]_8$  and the remaining samples. The effective Tb moment decreases due to the formation of a Tb-rich alloy contribution (Tb  $> 30$  at.%) in the ML.<sup>5,33</sup> This leads to a FeCo dominant sample at RT and the observed offset in magnetization.

Figure 3 shows MFM images and corresponding  $M$ - $H$  loops of the investigated samples depending on the annealing temperature. The MFM images in panel I were measured at RT in the as-deposited state after demagnetization. The images shown in the panels II and III were obtained at 570 and 720 K, respectively, followed by demagnetization at RT. The corresponding  $M$ - $H$  loops are shown underneath (panels IV-VI). The domain morphology in the equilibrium state can be used to make an assessment of changes in the magnetic properties, as the domain size depends on the uniaxial magnetic anisotropy  $K_u$ , saturation magnetization  $M_S$ , as well as the magnetic exchange stiffness  $A$ .<sup>62</sup> The magnetic domain size  $D$  can be estimated depending on the total film thickness  $t$  by

$$D(t) = t \cdot \exp\left(\frac{D_0}{t}\right), \quad (1)$$

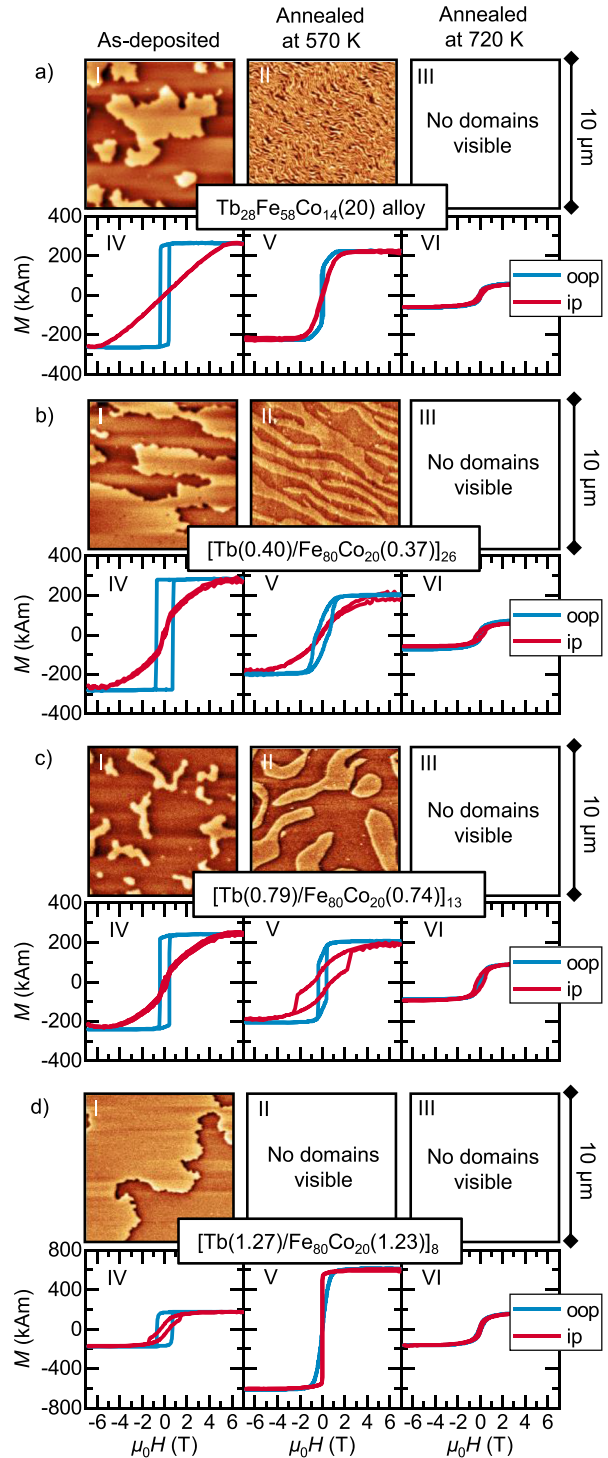


**FIG. 3.** In the first row of (a)–(d), MFM images are shown for three different annealing temperatures (panels I–III). The corresponding oop and ip  $M$ - $H$  loops are shown in panels IV–VI. The PMA of all samples decreases with annealing temperature. This is evident from both the size of the magnetic domains (panels I–II) and the  $M$ - $H$  loops (panels IV–VI). Note that no MFM contrast could be detected for some annealing temperatures (mainly for panels III).

with  $D_0$  being the ratio of the domain wall and magnetostatic energies, which is given by

$$D_0 = \frac{4\pi(AK_u)^{1/2}}{\mu_0 M_s^2}. \quad (2)$$

All samples in the as-deposited state reveal square loops with an easy axis of magnetization pointing in the oop direction (panels IV). In addition, only the sample with the thickest individual layers [Fig. 3(d-IV)] exhibits a pronounced hysteresis in the ip loop, indicating a more Tb-rich part (Tb > 30 at. %) of the ML with magnetic ip anisotropy. The  $M_s$  values of the loops are also comparable in all four samples before annealing with values between 180 and 290 kA/m. It is important to note that a different scale of  $M$  in Figs. 3(d-IV)–3(d-VI) is used and that the net magnetic moment in Fig. 3(d) is FeCo dominant in contrast to the Tb dominant moments in Figs. 3(a)–3(c), as revealed in Fig. 2. With the extracted  $K_u$  and  $M_s$  values [Figs. 4(a)–4(d)] from the  $M$ – $H$  loops and using an  $A$  value of  $10^{-12}$  J/m from the literature,<sup>63</sup> we can confirm the relation between the magnetic properties and the observed domain sizes via Eqs. (1) and (2). The estimated domain sizes are between 3 and 7  $\mu\text{m}$ , which agrees well with the experimentally observed domain structure.

Next, the samples were annealed at 570 K. While the alloy sample shows a strong loss in PMA [Fig. 3(a-V)], the MLs with the lowest layer thicknesses still reveal an oop easy axis magnetization [Figs. 3(b-V) and 3(c-V)]. This behavior is also reflected in the magnetic domain morphology presented in Figs. 3(a-II)–3(c-II). The domain size of the alloy sample decreases significantly more than that observed for the MLs. By inspecting the  $M$ – $H$  loops, it is clear that the pronounced loss in  $K_u$  is the main cause of the smaller domains observed in the alloy sample. The decrease in domain size is less significant for the MLs, especially for [Tb/Fe]<sub>13</sub>, due to a more resistant PMA. In contrast, the ML with the largest layer thickness reveals a clear ip magnetic anisotropy [Fig. 3(d-V)] with an almost tripled  $M_s$  value. This drastic rise cannot be explained by selective oxidation of the RE or TM layer or by an increased moment from crystalline phases. In this state, the Tb and FeCo moments appear to be strongly decoupled and align parallel with the applied field. Due to the ip magnetization of the sample, no contrast can be detected by MFM imaging, which is only sensitive to oop magnetic stray field gradients.

Annealing at 720 K resulted for all samples in a full loss of PMA as well as a strong decrease in  $M_s$ . These effects will be explained in more detail in Sec. III B.

In Fig. 4, the magnetic properties depending on the annealing temperature  $T_{\text{anneal}}$  are summarized. The saturation magnetization  $M_s$  [Fig. 4(a)], the magnetic coercive field  $H_c$  [Fig. 4(b)], and the effective magnetic anisotropy  $K_{\text{eff}}$  [Fig. 4(c)] were extracted from the  $M$ – $H$  loops. Positive  $K_{\text{eff}}$  values imply a magnetic oop easy axis, whereas negative ones imply an ip easy axis. The uniaxial magnetic anisotropy  $K_u$  was calculated by

$$K_u = K_{\text{eff}} + \frac{\mu_0}{2} M_s^2, \quad (3)$$

with  $\frac{\mu_0}{2} M_s^2$  being the magnetic shape anisotropy.

As mentioned before, all specimens have a similar  $M_s$  before annealing. With increasing  $T_{\text{anneal}}$ ,  $M_s$  of the alloy and the two

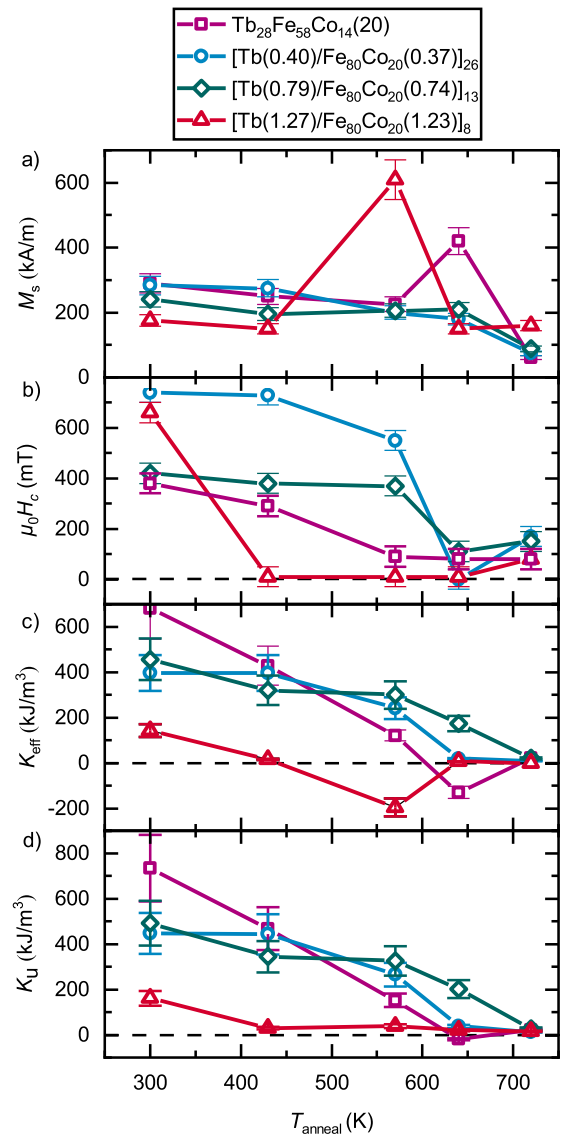


**FIG. 4.** Saturation magnetization  $M_s$  (a), coercivity  $H_c$  (b), effective magnetic anisotropy  $K_{\text{eff}}$  (c), and uniaxial magnetic anisotropy  $K_u$  (d) as a function of annealing temperature  $T_{\text{anneal}}$  measured at RT. The ML structure delays the transition from a magnetic oop anisotropy direction to an ip direction (dashed line in c) from 640 K (alloy) to 720 K ([Tb/FeCo]<sub>13</sub>). The magnetic properties of [Tb/FeCo]<sub>8</sub> differ greatly due to the individual layer thicknesses surpassing the critical intermixing thicknesses.

MLs with thinner individual layers decreases. Only at 640 K, the alloy exhibits a peak to nearly double its initial  $M_s$  value. A similar peak can be found for the ML with the thickest individual layers at 570 K. These peaks correspond to the only negative values of  $K_{\text{eff}}$  in Fig. 4(c). As described previously for [Tb/FeCo]<sub>8</sub> annealed at 570 K, the Tb and FeCo sub-lattices are assumed to be decoupled in this state that will be discussed in more detail later. The coercivity in Fig. 4(b) generally decreases with  $T_{\text{anneal}}$ , while the

coercive fields of  $[\text{Tb}/\text{FeCo}]_{26}$  and  $[\text{Tb}/\text{FeCo}]_{13}$  are more resilient to temperature.

The effective magnetic anisotropies of the as-deposited samples displayed in Fig. 4(c) reveal a difference between the MLs and the alloy. Different studies on similar systems<sup>9,64</sup> have reported an increase in  $M_s$  and  $K_{\text{eff}}$  for  $\text{Tb}(t_{\text{Tb}} < 1 \text{ nm})/\text{Fe}(t_{\text{Fe}} < 1 \text{ nm})$  ML structures in comparison to their alloy counterparts before annealing. The behavior of  $K_{\text{eff}}$  in Fig. 4(c) partially resembles the coercivity in Fig. 4(b). It decreases for all specimens, while the slopes of  $[\text{Tb}/\text{FeCo}]_{26}$  and  $[\text{Tb}/\text{FeCo}]_{13}$  are smaller than those of the rest. The alloy and  $[\text{Tb}/\text{FeCo}]_8$  exhibit an effective ip anisotropy at 570 and 640 K, respectively, which is primarily a result of their large  $M_s$  values and resulting shape anisotropy. At larger  $T_{\text{anneal}}$ , their  $K_{\text{eff}}$  values eventually also drop to zero.  $[\text{Tb}/\text{FeCo}]_8$  has a much smaller  $K_{\text{eff}}$  value than the other samples because of the previously discussed modulated Tb:FeCo ratio with Tb-rich layer parts. Figure 4(d) displays the  $K_u$  values in dependence of the annealing temperature. With increasing individual layer thicknesses, the loss in PMA is delayed from 640 K of the alloy to 720 K of  $[\text{Tb}/\text{FeCo}]_{13}$ . The layer thickness of  $[\text{Tb}/\text{FeCo}]_8$  is above the intermixing limit, resulting in a loss in PMA at already 420 K.

## B. Structural properties

Temperature dependent resistivity measurements were performed to investigate the structural changes in the alloy and MLs. Figure 5 shows the evolution of the electric sheet resistivity  $\sigma$  divided by the sheet resistivity  $\sigma_{0,\text{TbFeCo}}$  of the as-deposited  $\text{Tb}_{28}(\text{Fe}_{20}\text{Co}_{80})_{72}$  alloy sample upon annealing at a rate of 2 K/min. To give a better overview of the magnetic changes, exemplary  $M-H$  loops of  $[\text{Tb}/\text{FeCo}]_{26}$  are displayed above the resistivity curves. The loops are analogous to Figs. 3(b-IV)–3(b-VI). They were measured at RT, and the annealing temperature of the samples corresponds to the temperature marked with dashed lines in the diagram. The two MLs with smaller repetition numbers behave very similar to the alloy exhibiting a relative constant resistance up to 420 K. At higher temperatures, all samples show an increase in resistivity with a maximum at around 570 K, which is often associated with a structural relaxation of the film while still being amorphous.<sup>1,51,65,66</sup> This loss in chemical short-range order before crystallization is connected to the decrease in PMA seen in the first three loops displayed above the diagram and in Fig. 4(d). The drop of resistivity at temperatures larger than 570 K is associated with the beginning of diffusion and crystallization processes. All samples lose during these processes most of their remaining PMA. At about 700 K, a sharp rise in resistivity is observed, which can be explained by the crystallization of additional phases, oxidation, and formation of voids and discontinuities due to dewetting of the film. The magnetic properties drastically change at this point, revealing, besides a loss in PMA, a reduced magnetization [Fig. 4(a)].  $[\text{Tb}/\text{FeCo}]_8$  exhibits an overall smaller electrical resistivity due to its very FeCo dominated layers with lower electrical resistivities. The structural relaxation seems delayed in comparison to the other films' resistivity curves. This is typical for TbFeCo films with a larger FeCo ratio.<sup>51</sup> The curve is most likely a superposition of the more Tb-rich regions which might exhibit a structural relaxation at similar temperatures as the other samples and the relaxation of FeCo-rich regions responsible for the larger bump at higher temperatures. Still,  $[\text{Tb}/\text{FeCo}]_8$  lost all its PMA already at 420 K,

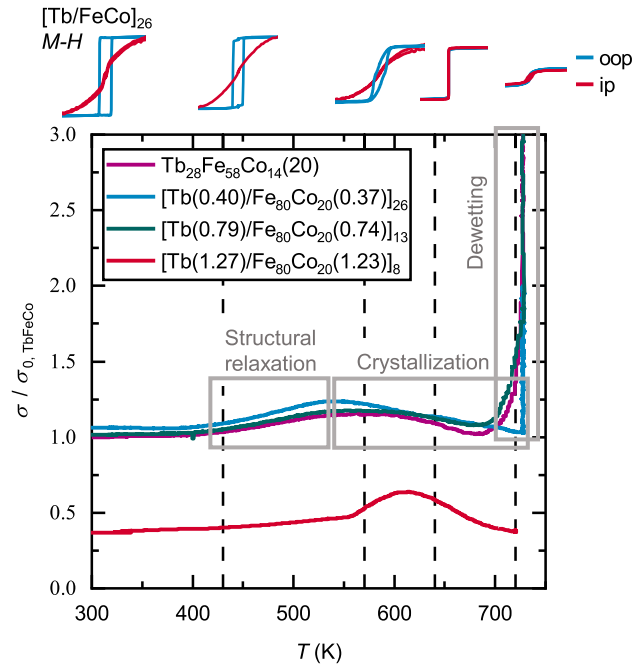


**FIG. 5.** The sheet resistivity  $\sigma$  divided by the sheet resistivity  $\sigma_{0,\text{TbFeCo}}$  of the  $\text{Tb}_{28}(\text{Fe}_{20}\text{Co}_{80})_{72}$  alloy as a function of annealing temperature  $T$  for all four sample types. Exemplary  $M-H$  loops of the  $[\text{Tb}/\text{FeCo}]_{26}$  ML are shown above their annealing temperatures marked by vertical dashed lines. The two MLs with thinner individual layers behave very similar to the alloy showing a bump at around 570 K, a decrease afterward, and a sharp rise above 700 K due to structural relaxation, crystallization, and dewetting, respectively.  $[\text{Tb}/\text{FeCo}]_8$  exhibits an overall smaller resistivity and no sharp increase at 700 K.

also because of the smaller initial PMA [Fig. 4(d)]. Furthermore, the dewetting of the film is not observable in the resistivity curve and shifted to higher temperatures, possibly due to the FeCo-rich regions of the film.

In order to achieve a better understanding of the structure of the MLs and the structural modifications upon annealing, exemplarily, the  $[\text{Tb}/\text{FeCo}]_8$  ML was investigated by TEM in the as-deposited state and after annealing at 640 K. Figure 6(a) shows a STEM cross-sectional image of the  $[\text{Tb}/\text{FeCo}]_8$  sample with the surface of the sample being on the left side. The two most bright layers on the left and right sides represent the roughly 5-nm-thick Pt cover and seed layer. The contrast in-between confirms the underlying Tb/FeCo ML structure. The purple arrow indicates the EDS linescan used to generate the composition map presented in Fig. 6(b), the  $x$  axis of which is aligned to the STEM image in (a). Overall, the resulting stack is slightly thicker than the intended 30 nm. The sputtered  $[\text{Tb}(1.27)/\text{Fe}_{80}\text{Co}_{20}(1.23)]_8$  film resulted in a modulation of the Tb and Fe ratio with a periodicity of 2.7 nm and relatively constant Co composition in the film. This means that the periodicity is 0.2 nm larger as intended by the nominal thickness. The modulation of Tb and Fe also supports the previously reported intermixing lengths of around 1 nm in these kinds of films.<sup>38,60</sup> The ML exhibits no sign of crystalline phases and appears to be amorphous in high-resolution TEM measurements (not shown). The modulation

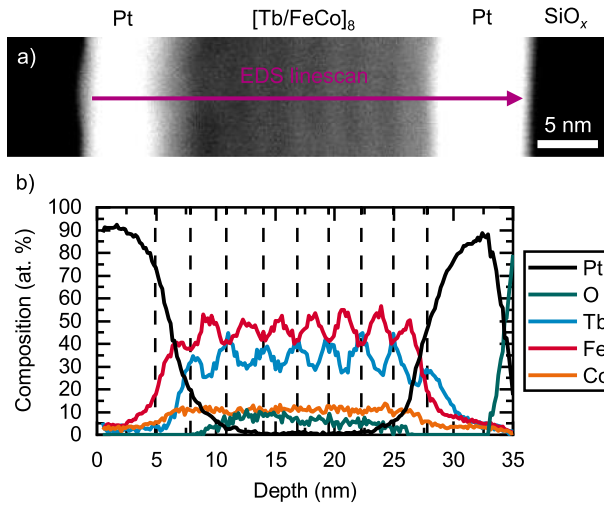


**FIG. 6.** STEM cross-sectional study of  $[\text{Tb}(1.27)/\text{Fe}_{80}\text{Co}_{20}(1.23)]_8$  in the as-deposited state. (a) STEM cross-sectional image in the as-deposited state confirming the ML structure. (b) Elemental EDS scans along the line marked in (a).

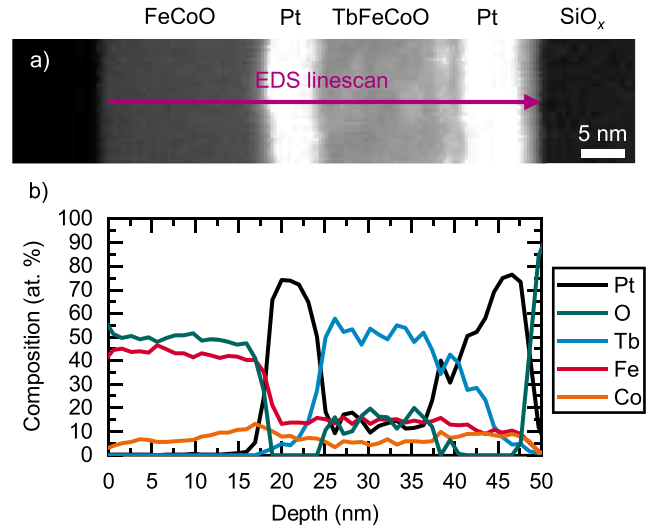


**FIG. 7.** STEM cross-sectional study of  $[\text{Tb}(1.27)/\text{Fe}_{80}\text{Co}_{20}(1.23)]_8$  after annealing at 640 K. (a) STEM cross-sectional image. (b) Elemental EDS scans along the line marked in (a). (c) High-resolution TEM image revealing nano-crystalline phases in the oxidized FeCo layer.

of Tb and Fe results in different compositions with  $\text{Tb}_{48}\text{Fe}_{41}\text{Co}_{11}$  and  $\text{Tb}_{26}\text{Fe}_{62}\text{Co}_{12}$  being the two extremes. This superposition of different compositions leads to an overall reduced Tb moment due to the reduced magnetization observed in Tb-rich alloy layers (Tb > 30 at. %),<sup>5,33</sup> agreeing with the experimental results. Also visible in the diagram is an oxygen contribution in the magnetic film that probably entered during preparation of the TEM sample. The sharp rise in oxygen on the right side arises from the  $\text{SiO}_x$  substrate. Note that the Si contribution is not displayed.

Figure 7 shows a STEM cross-sectional image (a), an EDS linescan (b), and an additional high-resolution TEM image (c) of the  $[\text{Tb}/\text{FeCo}]_8$  ML after annealing at 640 K. The ML structure of the film has fully vanished [Figs. 7(a) and 7(b)] due to intermixing processes. Surprisingly, a nearly 20-nm-thick layer appeared on top of the film. Figure 7(b) reveals that this new layer is primarily a mixture of Fe–Co–O. Consequently, Fe and Co have diffused through the Pt capping layer during annealing and got oxidized. The remaining alloy film in between the Pt layers became Tb-rich including a considerable amount of oxygen. While annealing induced phase separation has been observed before in these types of films,<sup>52,67</sup> this type of segregation was not expected.

To investigate the crystallinity of the layers, high-resolution TEM measurements were performed and one of the resulting images of the upper region of the film is displayed in Fig. 7(c). Both the Pt and the Fe–Co–O layers show a variety of crystalline grains with different orientations. The lattice plane distance of some of the larger grains in the Fe–Co–O layer of 0.27 nm corresponds most likely to hematite  $[\alpha\text{-Fe}_2\text{O}_3\text{-}0.273\text{ nm}(100)]$ .<sup>68</sup> This observed layer structure after annealing allows a clearer interpretation of the corresponding magnetic properties. As a result of strong diffusion, an Fe–Co–O layer has formed, which is well separated from the remaining Tb-rich alloy layer. This process results in a full loss in PMA [Fig. 4(d)]. The resulting Fe–Co–O layer is expected to be mostly

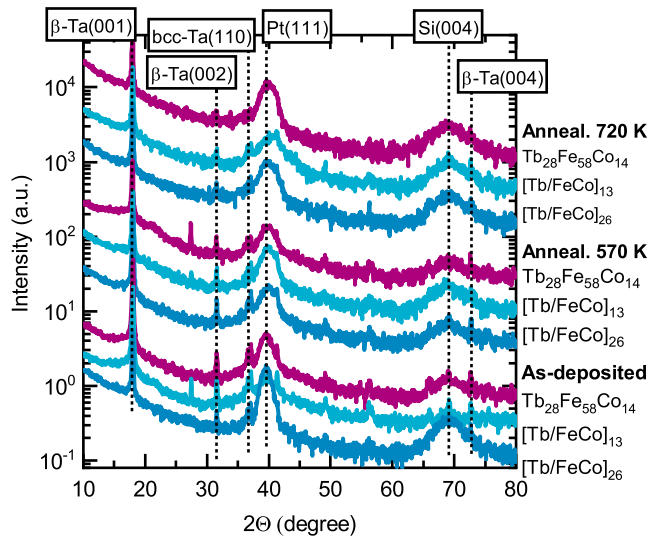


**FIG. 8.** XRD ( $\theta - 2\theta$ ) scans of  $\text{Tb}_{28}\text{Fe}_{58}\text{Co}_{14}(20)$ ,  $[\text{Tb}(0.40)/\text{Fe}_{80}\text{Co}_{20}(0.37)]_{26}$ , and  $[\text{Tb}(0.79)/\text{Fe}_{80}\text{Co}_{20}(0.74)]_{13}$  in the as-deposited state and after annealing at 570 and 720 K. There is no qualitative difference between the patterns of the pristine and annealed samples.

weakly ferromagnetic or even antiferromagnetic,<sup>69</sup> while the ferromagnetic Tb-rich alloy located in between the Pt layers exhibits reduced magnetization. Both effects eventually result in a drastic reduction in net magnetization, as observed experimentally [Fig. 4(a)]. Due to the continuous nature of this process, it is possible that we can obtain a state after annealing where the FeCo is already greatly separated and decoupled from the Tb, but not yet fully oxidized. Additionally, the remaining TbFeCo alloy can still contribute a substantial magnetic moment. This causes a pronounced increase in saturation magnetization, as observed in Fig. 4(a) at 570 K for the [Tb/FeCo]<sub>8</sub> ML and at 640 K for the alloy sample, respectively. Note that this effect is also expected for the other two samples but was not observed presumably due to the limited annealing steps.

In Fig. 8, the XRD  $\Theta - 2\Theta$  patterns of Tb<sub>28</sub>Fe<sub>58</sub>Co<sub>14</sub>(20), [Tb(0.40)/Fe<sub>80</sub>Co<sub>20</sub>(0.37)]<sub>26</sub>, and [Tb(0.79)/Fe<sub>80</sub>Co<sub>20</sub>(0.74)]<sub>13</sub> in the as-deposited state and after annealing at 570 and 720 K are shown. Except for the peaks of the substrate, capping, and seed layers, no peaks of the film can be observed. This contradicts the observations of  $\alpha$ -FeCo(110) peaks found at annealing temperatures higher than 650 K in other reported studies.<sup>1,51,66,70</sup> In addition, due to oxidation, Tb<sub>2</sub>O<sub>3</sub> can be formed.<sup>51</sup> We conclude that our films are in all states amorphous or nano-crystalline, as confirmed by TEM studies.

#### IV. CONCLUSION

We have investigated the magnetic and structural properties of Tb/FeCo multilayers and the corresponding alloy depending on annealing temperatures. First, we verified the magnetic Tb dominant nature showing rather similar temperature dependent magnetization curves for Tb<sub>28</sub>(Fe<sub>20</sub>Co<sub>80</sub>)<sub>72</sub>(20), [Tb(0.40)/Fe<sub>80</sub>Co<sub>20</sub>(0.37)]<sub>26</sub>, and [Tb(0.79)/Fe<sub>80</sub>Co<sub>20</sub>(0.74)]<sub>13</sub>. [Tb(1.27)/Fe<sub>80</sub>Co<sub>20</sub>(1.23)]<sub>8</sub> exhibited a very different behavior due to the composition modulation of the ML. Magnetic characterization revealed a decrease in perpendicular magnetic anisotropy and coercivity with increasing annealing temperature. We demonstrated that the annealing stability of TbFeCo alloys can be enhanced by the introduction of an artificial ML structure. The loss in PMA can be delayed from 640 K for the TbFeCo alloy to 720 K for the [Tb/FeCo]<sub>13</sub> ML. With four-point resistivity measurements, we linked the annealing temperature to the structural changes consisting of structural relaxation (loss in chemical short-range order), crystallization, and dewetting. Interestingly, upon annealing at higher temperatures, Fe and Co start to diffuse through the Pt cover layer, forming a well separated FeCo layer and leaving behind a Tb-rich TbFeCo alloy. This process results in a strong increase in the saturation magnetization until the sample gets fully oxidized.

These insights provide a better understanding of the changes in magnetic properties in Tb/FeCo multilayers depending on the layer structure upon annealing and set limits for the thermal stability, which will be beneficial for future high-temperature spintronic devices based on amorphous RE-TM materials.

#### ACKNOWLEDGMENTS

Financial support for this project was provided by the German Research Foundation (DFG, D.A.CH Project No. AL 618/24-1) and is gratefully acknowledged. M.K. was financially supported

by a postdoctoral fellowship provided by the Bavarian Research Foundation (Project No. PDOK-94-19).

#### DATA AVAILABILITY

The data that support the findings of this study are available from the corresponding author upon reasonable request.

#### REFERENCES

- S. Takayama, T. Niihara, K. Kaneko, Y. Sugita, and M. Ojima, *J. Appl. Phys.* **61**, 2610 (1987).
- C. J. Robinson, M. G. Samant, and E. E. Marinero, *Appl. Phys. A* **49**, 619 (1989).
- M. Tewes, J. Zweck, and H. Hoffmann, *J. Magn. Magn. Mater.* **95**, 43 (1991).
- V. G. Harris, K. D. Aylesworth, B. N. Das, W. T. Elam, and N. C. Koon, *Phys. Rev. Lett.* **69**, 1939 (1992).
- S. Yoshino, H. Takagi, S. Tsunashima, M. Masuda, and S. Uchiyama, *Jpn. J. Appl. Phys., Part 1* **23**, 188 (1984).
- S. Ota, P. Van Thach, H. Awano, A. Ando, K. Toyoki, Y. Kotani, T. Nakamura, T. Koyama, and D. Chiba, *Sci. Rep.* **11**, 6237 (2021).
- M. Krupinski, J. Hintermayr, P. Sobieszczyk, and M. Albrecht, *Phys. Rev. Mater.* **5**, 024405 (2021).
- S. C. N. Cheng and M. H. Kryder, *J. Appl. Phys.* **69**, 7202 (1991).
- N. Sato, *J. Appl. Phys.* **59**, 2514 (1986).
- E. F. Kneller and R. Hawig, *IEEE Trans. Magn.* **27**, 3588 (1991).
- M. Ungureanu, K. Dumesnil, C. Dufour, N. Gonzalez, F. Wilhelm, A. Smekhova, and A. Rogalev, *Phys. Rev. B* **82**, 174421 (2010).
- S. Romer, M. A. Marioni, K. Thorwarth, N. R. Joshi, C. E. Corticelli, H. J. Hug, S. Oezer, M. Parlinska-Wojtan, and H. Rohrmann, *Appl. Phys. Lett.* **101**, 222404 (2017).
- T. Hauet, F. Montaigne, M. Hehn, Y. Henry, and S. Mangin, *Phys. Rev. B* **79**, 224435 (2009).
- S. M. Watson, T. Hauet, J. A. Borchers, S. Mangin, and E. E. Fullerton, *Appl. Phys. Lett.* **92**, 202507 (2008).
- S. Mangin, T. Hauet, P. Fischer, D. H. Kim, J. B. Kortright, K. Chesnel, E. Arenholz, and E. E. Fullerton, *Phys. Rev. B* **78**, 024424 (2008).
- X. Zhao, A.-O. Mandru, C. Vogler, M. A. Marioni, D. Suess, and H. J. Hug, *ACS Appl. Nano Mater.* **2**, 7478 (2019).
- M. Heigl, C. Vogler, A.-O. Mandru, X. Zhao, H. J. Hug, D. Suess, and M. Albrecht, *ACS Appl. Nano Mater.* **3**, 9218 (2020).
- C. Vogler, M. Heigl, A.-O. Mandru, B. Hebler, M. Marioni, H. J. Hug, M. Albrecht, and D. Suess, *Phys. Rev. B* **102**, 014429 (2020).
- B. Dieny, V. S. Speriosu, S. S. Parkin, B. A. Gurney, D. R. Wilhoit, and D. Mauri, *Phys. Rev. B* **43**, 1297 (1991).
- F. Radu, R. Abrudan, I. Radu, D. Schmitz, and H. Zabel, *Nat. Commun.* **3**, 715 (2012).
- O. Redon and P. P. Freitas, *J. Appl. Phys.* **83**, 2851 (1998).
- C.-H. Lai, Z.-H. Wu, C.-C. Lin, and P. H. Huang, *J. Appl. Phys.* **97**, 10C511 (2005).
- J. Liao, H. He, Z. Zhang, B. Ma, and Q. Y. Jin, *J. Appl. Phys.* **109**, 023907 (2011).
- M.-S. Lin, C.-H. Lai, Y.-Y. Liao, Z.-H. Wu, S.-H. Huang, and R.-F. Jiang, *J. Appl. Phys.* **99**, 08T106 (2006).
- J. S. Moodera, L. R. Kinder, T. M. Wong, and R. Meservey, *Phys. Rev. Lett.* **74**, 3273 (1995).
- C. D. Stanciu, F. Hansteen, A. V. Kimel, A. Kirilyuk, A. Tsukamoto, A. Itoh, and T. Rasing, *Phys. Rev. Lett.* **99**, 047601 (2007).
- A. Hassdenteufel, B. Hebler, C. Schubert, A. Liebig, M. Teich, M. Helm, M. Aeschlimann, M. Albrecht, and R. Bratschitsch, *Adv. Mater.* **25**, 3122 (2013).
- B. Hebler, A. Hassdenteufel, P. Reinhardt, H. Karl, and M. Albrecht, *Front. Mater.* **3**, 8 (2016).
- A. Hassdenteufel, J. Schmidt, C. Schubert, B. Hebler, M. Helm, M. Albrecht, and R. Bratschitsch, *Phys. Rev. B* **91**, 104431 (2015).

- <sup>30</sup>T.-M. Liu, T. Wang, A. H. Reid, M. Savoini, X. Wu, B. Koene, P. Granitzka, C. E. Graves, D. J. Higley, Z. Chen, G. Razinskas, M. Hantschmann, A. Scherz, J. Stöhr, A. Tsukamoto, B. Hecht, A. V. Kimel, A. Kirilyuk, T. Rasing, and H. A. Dürr, *Nano Lett.* **15**, 6862 (2015).
- <sup>31</sup>T. Seifert, U. Martens, S. Günther, M. A. W. Schoen, F. Radu, X. Z. Chen, I. Lucas, R. Ramos, M. H. Aguirre, P. A. Algarabel, A. Anadón, H. S. Körner, J. Walowski, C. Back, M. R. Ibarra, L. Morellón, E. Saitoh, M. Wolf, C. Song, K. Uchida, M. Münzenberg, I. Radu, and T. Kampfrath, *SPIN* **07**, 1740010 (2017).
- <sup>32</sup>T. J. Huisman, C. Ciccarelli, A. Tsukamoto, R. V. Mikhaylovskiy, T. Rasing, and A. V. Kimel, *Appl. Phys. Lett.* **110**, 072402 (2017).
- <sup>33</sup>R. Schneider, M. Fix, R. Heming, S. Michaelis de Vasconcellos, M. Albrecht, and R. Bratschitsch, *ACS Photonics* **5**, 3936 (2018).
- <sup>34</sup>R. Schneider, M. Fix, J. Bensmann, S. Michaelis de Vasconcellos, M. Albrecht, and R. Bratschitsch, *Appl. Phys. Lett.* **115**, 152401 (2019).
- <sup>35</sup>M. Fix, R. Schneider, J. Bensmann, S. Michaelis de Vasconcellos, R. Bratschitsch, and M. Albrecht, *Appl. Phys. Lett.* **116**, 012402 (2020).
- <sup>36</sup>M. Fix, R. Schneider, S. Michaelis de Vasconcellos, R. Bratschitsch, and M. Albrecht, *Appl. Phys. Lett.* **117**, 132407 (2020).
- <sup>37</sup>F. Richomme, J. Teillet, A. Fnidiki, P. Auric, and P. Houdy, *Phys. Rev. B* **54**, 416 (1996).
- <sup>38</sup>K. Yamauchi, K. Habu, and N. Sato, *J. Appl. Phys.* **64**, 5748 (1988).
- <sup>39</sup>K. Cherifi, P. Donovan, C. Dufour, P. Mangin, and G. Marchal, *Phys. Status Solidi A* **122**, 311 (1990).
- <sup>40</sup>M. Nawate, K. Doi, and S. Honda, *J. Magn. Magn. Mater.* **126**, 279 (1993).
- <sup>41</sup>J. Tappert, F. Klose, C. Rehm, W. S. Kim, R. A. Brand, H. Maletta, and W. Keune, *J. Magn. Magn. Mater.* **157-158**, 317 (1996).
- <sup>42</sup>S. Honda, M. Nawate, and I. Sakamoto, *J. Appl. Phys.* **79**, 365 (1996).
- <sup>43</sup>F. Richomme, A. Fnidiki, P. Auric, J. Teillet, P. Boher, and P. Houdy, *Hyperfine Interact.* **92**, 1243 (1994).
- <sup>44</sup>L. Avilés-Félix, A. Olivier, G. Li, C. S. Davies, L. Álvaro-Gómez, M. Rubio-Roy, S. Auffret, A. Kirilyuk, A. V. Kimel, T. Rasing, L. D. Buda-Prejbeanu, R. C. Sousa, B. Dieny, and I. L. Prejbeanu, *Sci. Rep.* **10**, 5211 (2020).
- <sup>45</sup>L. Avilés-Félix, L. Farcis, Z. Jin, L. Álvaro-Gómez, G. Li, K. T. Yamada, A. Kirilyuk, A. V. Kimel, T. Rasing, B. Dieny, R. C. Sousa, I. L. Prejbeanu, and L. D. Buda-Prejbeanu, *Sci. Rep.* **11**, 6576 (2021).
- <sup>46</sup>S. A. Montoya, S. Couture, J. J. Chess, J. C. T. Lee, N. Kent, D. Henze, S. K. Sinha, M. Y. Im, S. D. Kevan, P. Fischer, B. J. McMorrán, V. Lomakin, S. Roy, and E. E. Fullerton, *Phys. Rev. B* **95**, 024415 (2017).
- <sup>47</sup>M. Heigl, S. Koraltan, M. Vaňatka, R. Kraft, C. Abert, C. Vogler, A. Semisalova, P. Che, A. Ullrich, T. Schmidt, J. Hintermayr, D. Grundler, M. Farle, M. Urbánek, D. Suess, and M. Albrecht, *Nat. Commun.* **12**, 2611 (2021).
- <sup>48</sup>S. S. P. Parkin, M. Hayashi, and L. Thomas, *Science* **320**, 190 (2008).
- <sup>49</sup>S. Emori, U. Bauer, S.-M. Ahn, E. Martinez, and G. S. D. Beach, *Nat. Mater.* **12**, 611 (2013).
- <sup>50</sup>P. Hansen, C. Clausen, G. Much, M. Rosenkranz, and K. Witter, *J. Appl. Phys.* **66**, 756 (1989).
- <sup>51</sup>K. Wang, S. Dong, Y. Huang, and Y. Qiu, *J. Magn. Magn. Mater.* **434**, 169 (2017).
- <sup>52</sup>R. Ranchal, E. López, J. L. Prieto, and C. Aroca, *Acta Mater.* **59**, 2865 (2011).
- <sup>53</sup>R. Ranchal, J. L. Prieto, P. Sánchez, and C. Aroca, *J. Appl. Phys.* **107**, 113918 (2010).
- <sup>54</sup>L.-X. Ye, R. C. Bhatt, C.-M. Lee, S.-M. Chang, and T.-h. Wu, *AIP Adv.* **9**, 125316 (2019).
- <sup>55</sup>R. C. Bhatt, L.-X. Ye, and T.-h. Wu, *J. Magn. Magn. Mater.* **498**, 166159 (2020).
- <sup>56</sup>S. Q. Yin, X. Q. Li, X. G. Xu, J. Miao, and Y. Jiang, *IEEE Trans. Magn.* **47**, 3129 (2011).
- <sup>57</sup>W. Cheng, X. Miao, J. Yan, and G. Lin, *Proc. SPIE* **7125**, 71250U (2009).
- <sup>58</sup>S. C. Shin, *J. Appl. Phys.* **61**, 3340 (1987).
- <sup>59</sup>A.-O. Mandru, O. Yildirim, M. A. Marioni, H. Rohrmann, M. Heigl, O.-T. Ciubotariu, M. Penedo, X. Zhao, M. Albrecht, and H. J. Hug, *J. Vac. Sci. Technol. A* **38**, 023409 (2020).
- <sup>60</sup>Y. Fujiwara, X. Y. Yu, S. Tsunashima, S. Iwata, M. Sakurai, and K. Suzuki, *J. Appl. Phys.* **79**, 6270 (1996).
- <sup>61</sup>W.-S. Kim, W. Andrä, and W. Kleemann, *Phys. Rev. B* **58**, 6346 (1998).
- <sup>62</sup>B. Kaplan and G. A. Gehring, *J. Magn. Magn. Mater.* **128**, 111 (1993).
- <sup>63</sup>S. Mangin, F. Montaigne, and A. Schuhl, *Phys. Rev. B* **68**, 140404 (2003).
- <sup>64</sup>J. Pommier, J. P. Jamet, J. Ferré, P. Houdy, P. Boher, and F. Pierre, *J. Magn. Magn. Mater.* **136**, 251 (1994).
- <sup>65</sup>V. A. Blagojević, M. Vasić, B. David, D. M. Minić, N. Pizurova, T. Žák, and D. M. Minić, *Mater. Chem. Phys.* **145**, 12–17 (2014).
- <sup>66</sup>E. Yüzüak, G. D. Yüzüak, and A. Hütten, *J. Alloys Compd.* **863**, 158088 (2020).
- <sup>67</sup>P. J. Grundy, E. T. M. Lacey, and C. D. Wright, *J. Magn. Magn. Mater.* **54-57**, 227 (1986).
- <sup>68</sup>U. Schwertmann and R. M. Cornell, “Crystal structure,” in *The Iron Oxides* (John Wiley & Sons, 2003), Chap. 2, pp. 9–38.
- <sup>69</sup>U. Schwertmann and R. M. Cornell, “Electronic, electrical and magnetic properties and colour,” in *The Iron Oxides* (John Wiley & Sons, 2003), Chap. 6, pp. 111–137.
- <sup>70</sup>K. Umadevi, M. Palit, J. A. Chelvane, D. A. Babu, A. P. Srivastava, S. V. Kamat, and V. Jayalakshmi, *J. Supercond. Novel Magn.* **29**, 2455–2460 (2016).